

A pseudopotential study of electron-hole excitations in colloidal, free-standing InAs quantum dots

A. J. Williamson and Alex Zunger

National Renewable Energy Laboratory, Golden, CO 80401

(September 8, 2018)

Abstract

Excitonic spectra are calculated for free-standing, surface passivated InAs quantum dots using atomic pseudopotentials for the single-particle states and screened Coulomb interactions for the two-body terms. We present an analysis of the single particle states involved in each excitation in terms of their angular momenta and Bloch-wave parentage. We find that (i) in agreement with other pseudopotential studies of CdSe and InP quantum dots, but in contrast to $k.p$ calculations, dot states wavefunction exhibit strong odd-even angular momentum envelope function mixing (e.g. s with p) and large valence-conduction coupling. (ii) While the pseudopotential approach produced very good agreement with experiment for free-standing, colloidal CdSe and InP dots, and for self-assembled (GaAs-embedded) InAs dots, here the predicted spectrum does *not* agree well with the measured (ensemble average over dot sizes) spectra. (1) Our calculated excitonic gap is larger than the PL measured one, and (2) while the spacing between the lowest excitons is reproduced, the spacings between higher excitons is not fit well. Discrepancy (1) could result from surface states emission. As for (2), agreement is improved when account is taken of the finite size distribution in the experimental data. (iii) We find that the single particle gap scales as $R^{-1.01}$ (not R^{-2}), that the screened (unscreened) electron-hole Coulomb interaction scales as $R^{-1.79}$ ($R^{-0.7}$), and

that the excitonic gap scales as $R^{-0.9}$. These scaling laws are different from those expected from simple models.

PACS:73.20.-r, 73.20.Dx, 85.30.Vw

I. INTRODUCTION

Semiconductor quantum [1] dots have recently generated considerable interest due to the dramatic differences between their electronic structure and that of the bulk material from which they are derived. These differences arise from the lower symmetry of the dot, quantum confinement level shifts and the enhancement of electron hole Coulomb and exchange interactions.

While the Stranski-Krastanov growth technique produces semiconductor-embedded dots [2–4] which are typically subject to only a small confining potential, colloidal chemistry techniques [5–7] produce dots whose surfaces are passivated by large organic molecules. This leads to much larger confining potentials (a few eV), and thus many more confined energy levels. These colloidal techniques have recently enabled the production of quantum dots with diameters from 10 to 60Å , made from CdSe [8], CdS [9], InP [10] and InAs [11]. The spectroscopy of these systems is richer than that of the SK dots, with several groups reporting data for up to 10 excited states in CdSe [8], InP [10] and InAs [11]. On the theoretical side, colloidal CdSe [8,12] and InP [10,13] have recently been studied using both the standard 6x6 k.p method [8,10] and more sophisticated pseudopotential [14,13,12] techniques.

In this paper we turn our attention to colloidal grown InAs quantum dots. InAs is a challenging system to study because, (i) the small bulk band gap of 0.42 eV suggests strong valence-conduction band coupling. This is supported by recent studies [11,15] showing that the standard 6x6 k.p formalism fails to describe the observed electronic transitions, while 8x8 k.p produces a better fit to measured excitonic transitions, (ii) the small band gap combined with a large spin-orbit splitting (0.38 eV) suggests that spin orbit effects will play a significant role, (iii) the observed band gap extends to 1.6 eV, i.e. almost four times the bulk value, suggesting dramatic quantum confinement, (iv) the large confining potential leads to as many as eight clearly resolved excitations, for a range of dot sizes.

We use a multi-band pseudopotential Hamiltonian to calculate both the single particle

states and electron-hole excitation energies for InAs quantum dots with a range of sizes. Our method is different from another recent pseudopotential calculation of Mizel and Cohen [15] in that although their formalism can be generalized to multiple bands, they use only a single-band approximation (like the EMA or the Truncated Crystal Method [16]) and do not include electron-hole effects. Both methods however, do incorporate non-parabolicity of the bands. The nature of the single particle states is analyzed in terms of the parent Bloch orbitals and envelope functions, which enables a detailed description of the origin of each calculated exciton. This analysis allows comparisons to be made with existing effective mass based predictions for the single particle states in these dots. In contrast to envelope function based effective mass calculations, our more general treatment shows that the single particle states include a significant amount of mixing of valence and conduction states, as well as a mixing of envelope functions with odd and even parity. We have calculated the *single dot* absorption spectra of a few dots. Comparing with the experimental results for ensembles of dots sizes, we do not find good agreement in contrast to the k.p method [11] that gives better agreement. However, agreement with our results is improved when the finite size distribution of the experimental dot samples is taken into account. We discuss possible reasons for the conflicts between experiment and theory.

II. PSEUDOPOTENTIAL CALCULATIONS OF THE ELECTRONIC STRUCTURE OF INAS QUANTUM DOTS

Our pseudopotential calculations consist of two steps. First we calculate the single particle states for the quantum dot (Sections. II A and II B). Then we solve the “two-particle” problem by calculating the energy of the electron-hole excitations of the system (Section. II C).

A. Single Particle Calculation

We use a pseudopotential Hamiltonian to model the single-particle electronic structure of the system.

$$\hat{H} = -\frac{1}{2}\nabla^2 + \sum_{\alpha,n} v_{\alpha}(\mathbf{r} - \mathbf{R}_{\alpha n}) + v_{\alpha}^{(SO)} . \quad (1)$$

The system's potential is constructed from a sum of screened atomic pseudopotentials, v_{α} , where α represents In and As, and $\mathbf{R}_{\alpha n}$ are the positions of the In and As atoms within the dot. The pseudopotentials, v_{α} , have been fitted to the experimental band gaps and effective masses of bulk InAs. The experimental and fitted values are given in Table I. The fitted InAs bulk band structure is shown in Fig. 1. We use the reciprocal space functional form of the pseudopotential

$$v_{\alpha}(\mathbf{q}) = a_{0\alpha} \frac{(q^2 - a_{1\alpha})}{a_{2\alpha} e^{a_{3\alpha} q^2} - 1} , \quad (2)$$

where $a_{0\alpha}, a_{1\alpha}, a_{2\alpha}, a_{3\alpha}$ are adjustable parameters. The fitted values of $a_{i,\alpha}$ are given in Table II. The same pseudopotential form was recently used to study self-assembled GaAs-covered InAs pyramidal dots [17–20]. In Refs. [17–20] the pseudopotential contained an additional term to describe the effects of strain in the system. As the free-standing InAs dots studied here are strain free this term is not required here. We assume the bulk zinc-blende structure and the bulk In-As inter-atomic spacing ($d=6.057\text{\AA}$). We construct spherical InAs dots of radius R , by selecting all the atoms that fall within a sphere of this radius. Any atoms from the surface of the dot which have three dangling bonds are removed. The result of adopting this atomistic description is to reduce the symmetry of the dots from the full spherical symmetry of continuum models to the lower T_d symmetry. The sizes and compositions of the four dots studied in this paper are listed in Table III.

To simulate the chemical passivation via ligands [7], we embed the InAs dots within an artificial barrier material, represented by an atomic pseudopotential, fitted to have a larger band gap than InAs, thus producing a type-I alignment between the dot and the barrier. The

barrier material is designed to have the InAs lattice constant so that no strain is introduced into the system. This embedding process is physically equivalent to the choice of a finite barrier surrounding the dots and is designed to reflect the fact that the dots are surrounded by organic molecules which themselves have large, but finite band gaps [21].

We expand the single particle wavefunctions, ψ_i , in a plane wave basis whose cutoff must be identical to that used in the original pseudopotential generating procedure,

$$\psi_i(\mathbf{r}) = \sum_{\mathbf{G}}^{E_{cut}} c_{\mathbf{G},i} e^{i\mathbf{G} \cdot \mathbf{r}} . \quad (3)$$

The matrix elements of the Hamiltonian in Eq.(1) in the basis of Eq.(3) are calculated according to

$$\hat{H}_{\mathbf{G},\mathbf{G}'} = \frac{1}{2} \mathbf{G}^2 \delta_{\mathbf{G},\mathbf{G}'} + V_{local}(\mathbf{G} - \mathbf{G}') + V_{nonlocal}(\mathbf{G}, \mathbf{G}') . \quad (4)$$

The spin orbit interaction is represented by a non-local pseudopotential, $V_{nonlocal}(\mathbf{G}, \mathbf{G}')$, which is evaluated in real space using the linearly scaling small box method from Ref. [22]. This method applies the non-local pseudopotential to each atom in turn. For each atom, a new wavefunction $\psi_{box}(\mathbf{r}) = \psi_i(\mathbf{r})$ is defined within a small box around the atom. $\psi_{box}(\mathbf{r})$ is periodically repeated and then fast Fourier transforms are used to generate $\psi_{box}(\mathbf{G})$. The non-local pseudopotential is then applied by

$$\phi_i(\mathbf{G}) = \sum_{\mathbf{G}'} V_{nonlocal}(\mathbf{G}, \mathbf{G}') \psi_{box}(\mathbf{G}') . \quad (5)$$

The InAs dots, surrounded by barrier material, form a supercell which is periodically repeated. Sufficient barrier atoms are used, to ensure that the interactions between an InAs dot and its periodic images are negligible. The total number of atoms (In, As and barrier) in the largest supercell is 25,000 atoms, which is too large for the Hamiltonian in Eq.(1) to be solved by conventional diagonalization methods. We thus use the “Folded Spectrum Method” (FSM) [23,24], in which one solves for the eigenstates of the equation

$$(\hat{H} - \epsilon_{ref})^2 \psi_i = (\epsilon - \epsilon_{ref})^2 \psi_i , \quad (6)$$

where ϵ_{ref} is a reference energy. By placing ϵ_{ref} within the band gap of the dot, and close to the valence band maximum or conduction band minimum, one is then able to obtain the top few valence states or the bottom few conduction states respectively by minimizing $\langle \psi | (H - E_{ref})^2 | \psi \rangle$. The use of FFTs results in an $N \ln N$ scaling with the number of atoms, N , enabling calculation of systems containing 10^5 atoms. It is easy to guess an approximate value of ϵ_{ref} : We first determine the position of the *bulk* InAs band edges by using the same pseudopotential to calculate the bulk InAs band structure, ϵ_{nk} . This is illustrated in Fig.1. As quantum confinement effects push electron(hole) levels up(down) in energy, placing ϵ_{ref} within the bulk band gap ensures that it will also be within the band gap of the InAs dot. Note, that although Eq.(6) has twice as many eigensolutions as the standard Schrödinger equation, $\hat{H}\psi_i = \epsilon_i \psi_i$, we only search for solutions to Eq.(6) in a finite basis of N plane waves [Eq.(3)]. We therefore only have N solutions to Eq.(6). By applying the \hat{H} operator twice, it can be shown that each of these N solutions is a solution of $\hat{H}\psi_i = \epsilon_i \psi_i$ and thus all our solutions to Eq.(6) are also solutions of the standard Schrödinger equation. Note also that our approach to the single-particle problem includes [Eq.(1)] shape effects, interface effects and spin-orbit coupling in the Hamiltonian [Eq.(1)]. In the effective mass approximation, on the other hand, these effects are included perturbatively [11]. Also note that we neglect self-consistency with respect to the bulk. As the dots contain several hundred atoms we expect the potential of the dot interior to be bulk-like. The pseudopotential used here was fitted to reproduce these bulk properties without requiring a self-consistent calculation.

B. Methods for analyzing the single particle wavefunctions

Having calculated the single particle states of an InAs quantum dot, we are interested in analyzing the nature of each of these states in terms of the bulk Bloch wavefunctions $\{\phi_{nk}\}$ from which they are derived, the symmetry of their envelope functions and their defining quantum numbers. These quantities will enable us to classify each of the electron-hole excitations calculated in the following section in terms of the detailed nature of their

initial valence state and the final conduction state. They also enable us to make contact with alternative electronic structure theories, such as the k.p technique, which typically classifies states in terms of their envelope function and total angular momentum. Note, the expressions in Eqs.(7)-(10) below are used only to analyse the solutions of Eq.(3) and do not affect the results.

We first deconstruct each single particle dot wavefunction, $\psi_i(\mathbf{r})$, in terms of the bulk Bloch states at the Γ point, $\phi_{n\Gamma} = u_{n\Gamma}(\mathbf{r})e^{i\mathbf{k}\cdot\mathbf{r}}$ in the manner described in Ref. [12]. We choose this basis to (i) enable the calculation of the different angular momentum character of the states, and (ii) to enable comparison with conventional envelope function based methods. These zone center Bloch states form a complete set, and therefore one can expand the single particle dot wavefunction according to

$$\psi_i(\mathbf{r}) = \sum_n \left[\sum_{\mathbf{k}} b_n(\mathbf{k}) e^{i\mathbf{k}\cdot\mathbf{r}} \right] u_{n,\Gamma}(\mathbf{r}) \quad (7)$$

which can be rewritten as

$$\psi_i(\mathbf{r}) = \sum_n u_{n,\Gamma}(\mathbf{r}) f_n^{(i)}(\mathbf{r}) \quad , \quad (8)$$

where $u_{n,\Gamma}(\mathbf{r})$ is the bulk Bloch wavefunction for the n th band at the Γ point, and $f_n^{(i)}(\mathbf{r})$ is a corresponding envelope function. Note that the “single band approximation” corresponds to retaining a single n value in Eq.(8), while the 6x6 k.p corresponds to $n = \text{bulk VBM}$ (sixfold degenerate, including spin). The present “multiband” method corresponds to a large number of bands in Eq.(8). We further decompose each envelope function, $f_n^{(i)}(\mathbf{r})$, into spherical harmonics, $Y_{L,m}(\theta, \phi)$, according to,

$$f_n^{(i)}(\mathbf{r}) = \sum_{L,m} R_{n,L,m}^{(i)}(|\mathbf{r}|) Y_{L,m}(\theta, \phi) \quad , \quad (9)$$

and then define the weight from each angular momentum component, $w_{n,L}^{(i)}$, as

$$w_{n,L}^{(i)} = \sum_{m=-L}^L \int_0^R |r R_{L,m}^n(r)|^2 dr \quad , \quad (10)$$

where R is the radius of the quantum dot. The quantity, $w_{n,L}^{(i)}$, tells us how much of bulk band n and angular momentum L is contained in the dot wavefunction ψ_i .

An additional property that is useful for classifying the single particle states is the total angular momentum, F , of dot state i . This is calculated for each of the single particle dot states according to

$$F(F+1) = \left\langle \sum_n u_{n,\Gamma} f_n^{(i)} | (\hat{F}_u + \hat{F}_f)^2 | \sum_m u_{m,\Gamma} f_m^{(i)} \right\rangle . \quad (11)$$

The angular momentum operator $\hat{F}_u = i\mathbf{r} \times \nabla + \vec{s}$, (where \vec{s} is the Dirac spin matrix), acts only on the Bloch orbitals, $u_n(\mathbf{r})$, and $\hat{F}_f = i\mathbf{r} \times \nabla$ acts only on the envelope function, $f_n^{(i)}(\mathbf{r})$.

C. Two particle calculation and the absorption spectrum

Calculation of an optical absorption spectrum based on the single particle states of a quantum dot, requires a solution for the “two-body” electron-hole problem. More complete solutions of the electron-hole problem via the configuration interaction require knowledge of the Coulomb, exchange and correlation energy associated with the electron-hole pair [25]. In this work, we choose to ignore the fine structure effects resulting from the exchange and correlation energy, reducing the two-body problem simply to calculating the electron-hole Coulomb energy. We then define the exciton energy in terms of the initial single particle valence state energy, ϵ_i , the final conduction state energy, ϵ_j , and the electron-hole Coulomb energy, J_{ij} , as

$$E_{exciton}^{(ij)} = (\epsilon_j - \epsilon_i) - J_{ij} . \quad (12)$$

The electron-hole Coulomb energy, J_{ij} , between each of the possible electron(i) - hole(j) pairs is calculated by a direct integration of the single particle wavefunctions

$$J_{ij}(R) = \int \int \frac{|\psi_i(\mathbf{r}_1)|^2 |\psi_j(\mathbf{r}_2)|^2}{\bar{\epsilon}(\mathbf{r}_1 - \mathbf{r}_2; R) |\mathbf{r}_1 - \mathbf{r}_2|} d\mathbf{r}_1 d\mathbf{r}_2 \propto R^{-n}, \quad (13)$$

where $\psi_i(\mathbf{r})$ and $\psi_j(\mathbf{r})$ are our calculated electron and hole wavefunctions and $\bar{\epsilon}(\mathbf{r}_1 - \mathbf{r}_2, R)$ is a distance dependent screening function, connected to the dielectric function, $\epsilon(\mathbf{r}, \mathbf{r}', R)$, by,

$$\frac{1}{\bar{\epsilon}(\mathbf{r}, \mathbf{r}'')} \frac{1}{|\mathbf{r} - \mathbf{r}''|} = \int d\mathbf{r}' \epsilon^{-1}(\mathbf{r}, \mathbf{r}'; R) \frac{1}{|\mathbf{r}'' - \mathbf{r}'|} \quad (14)$$

and n is a size scaling exponent discussed below. We follow Ref. [12] in writing the Fourier transform of $\epsilon^{-1}(\mathbf{r}_1 - \mathbf{r}_2; R)$ as the sum of electronic and ionic terms,

$$\epsilon^{-1}(k; R) = \epsilon_{el}^{-1}(k; R) + \Delta\epsilon_{ion}^{-1}(k; R) \quad , \quad (15)$$

The electronic term is defined in terms of the Thomas Fermi model of Resta [26],

$$\epsilon_{el}^{-1}(k; R) = \frac{k^2 + q^2 \sin(kR_\infty) / (\epsilon_\infty^{dot} k R_\infty)}{k^2 + q^2} \quad . \quad (16)$$

Note, the R dependence of $\epsilon_{el}^{-1}(k; R)$ comes from ϵ_∞^{dot} . We define q in Eq.(16) as

$$q = 2\pi^{-1/2} (3\pi^2 n_0)^{1/3} \quad , \quad (17)$$

where n_0 is the electron density, and R_∞ is the solution to

$$\frac{\sinh(qR_\infty)}{qR_\infty} = \epsilon_\infty^{dot} \quad . \quad (18)$$

The ionic term is taken from Ref. [27]

$$\Delta\epsilon_{ion}^{-1}(k; R) = \left(\frac{1}{\epsilon_0^{dot}} - \frac{1}{\epsilon_\infty^{dot}} \right) \left(\frac{1/2}{1 + \rho_h^2 k^2} + \frac{1/2}{1 + \rho_e^2 k^2} \right) \quad . \quad (19)$$

Here $\rho_{h,e} = (2m_{h,e}^* \omega_{LO}/\hbar)^{-1/2}$, ω_{LO} is the longitudinal optical-phonon frequency (238.6 cm^{-1}) and $m_{h,e}^*$ are the electron and hole effective masses (0.023 and 0.4 m_0). To obtain the value of ϵ_0^{dot} , we again assume that the dot interior is bulk-like so $\epsilon_0^{dot} - \epsilon_\infty^{dot}$ can be approximated from the bulk,

$$\epsilon_0^{dot} - \epsilon_\infty^{dot} = \epsilon_0^{bulk} - \epsilon_\infty^{bulk} = \Delta\epsilon_{ion}^{bulk} \quad . \quad (20)$$

We use the bulk value of 2.9 for $\Delta\epsilon_{ion}^{bulk}$. Finally, we use a generalization [28] of the Penn model [29] to obtain ϵ_∞^{dot} ,

$$\epsilon_\infty^{dot}(R) = 1 + (\epsilon_\infty^{bulk} - 1) \frac{(E_{gap}^{bulk} + \Delta)^2}{(E_{gap}^{dot}(R) + \Delta)^2} \quad , \quad (21)$$

where $\Delta = E_2 - E_{gap}^{bulk} = 4.28$ eV. The electronic and ionic components of the screening function are plotted in Figs. 2(a) and (b). One sees that the electronic contribution dominates for all but the smallest k -vectors. Figure 3 shows the screened dielectric function in real space, $\epsilon(R, r)$, as a function of electron-hole separation r , for dots with radii, R , from Table III. At very small separations, $\epsilon(R, r)$ approaches 1.0, which corresponds to no screening at zero separation between the electron and hole. When the electron and hole are separated by $r = 6 - 8\text{\AA}$, $\epsilon(r)$ approaches the particular value of $\epsilon_\infty^{dot}(R)$ which is different for each of the dots : The resulting values of $\epsilon_\infty^{dot}(R)$ are 7.19, 7.91, 8.41 and 8.92 for dot diameters 23.9, 30.3, 36.6 and 42.2\AA. The ionic screening, $\Delta\epsilon_{ion}$ has a very long tail, such that $\epsilon(r)$ approaches ϵ_0^{dot} for $r > 100\text{\AA}$. The R-dependence of $\epsilon(r, R)$ can be clearly seen in Fig. 3. In all cases the value is smaller than the bulk InAs value of $\epsilon_0^{bulk} = 15.15$.

More simplified calculations of J_{ij} assume a universal value for all i and j , based on an s -like envelope function and an infinite potential barrier [30]. These approximations lead to the often adopted formula

$$J^{EMA} = \frac{-3.572}{\epsilon_0^{bulk} 2R} \propto R^{-1}. \quad (22)$$

Our pseudopotential calculated values for the screened electron-hole Coulomb energy between an electron in the lowest energy conduction state and a hole in the highest energy valence state, J_{11} , are plotted along with those predicted by Eq.(22) in Fig. 4. The magnitude of the pseudopotential values is larger than that predicted by Eq.(22) for all sizes of dot. A fit of the dependence of the screened Coulomb energies, J , on the dot radius, R , to $J = A/R^n$, yields a size exponent, n , of 1.79, for the pseudopotential results, compared to the 1.0 scaling predicted by the Eq.(22). The difference in magnitude between Eq.(22) and pseudopotential calculated Coulomb energies of Eq.(13) has two sources: Firstly, we use microscopic (rather than envelope) functions that are not required to vanish exactly on the surface of the dot as EMA functions are required to do when subjected to an infinite potential barrier. This wavefunction effect causes the unscreened Coulomb energy ϵJ to scale as R^{-m} with $m < 1$, while in the EMA $m = 1$. This effect was discussed by Franceschetti *et al.*

al. [31] who found $m \sim 0.7$ for GaAs. Secondly, the description of screening in Eqs.(14) to (21) leads to a reduced screening at small R with respect the bulk screening, ϵ_0^{bulk} . This acts to *increase* our values of J_{ij} and its R dependence with respect to those in Eq.(22). This effect is opposite and stronger than the wavefunction effect. The net effect is $J \sim R^{-1.79}$ compared with $J \sim R^{-1}$ in Eq.(22). The present calculated values for the size scaling of the unscreened electron-hole Coulomb interaction, ϵJ , and the screened Coulomb interaction, J for InAs dots are compared with calculations for Si [39], InP [38] and CdSe [12] dots as well as the predictions from Eq.(22) in Table IV. It shows that for the scaling of ϵJ has $m < 1$ while the scaling of J has $n > 1$.

The final stage in the calculation of our theoretical absorption spectra, is to calculate the dipole matrix transition element for the transition from valence state i to conduction state j , $M_{i \rightarrow j}$,

$$M_{i \rightarrow j}(R) = |\langle \psi_i | \nabla | \psi_j \rangle|^2 \quad . \quad (23)$$

The optical absorption spectra, $I(E, R)$, can then be written as,

$$I(E, R) = \sum_i \sum_j M_{i \rightarrow j}(R) \exp \left[- \left(\frac{E - E_{exciton}^{(ij)}}{\sigma} \right)^2 \right] \quad , \quad (24)$$

where $E_{exciton}^{(ij)}$ is the excitation energy [Eq.(12)] and σ represents an experimental linewidth broadening which we set to 25 meV.

Our theory of Eq.(24) corresponds to the spectra of a single dot with a well defined radius, R , and shape. Current samples exhibit a size distribution about an average size, \bar{R} , producing an ensemble absorption spectra

$$\bar{I}(E, \langle R \rangle) = \int P(R) I(E, R) dR \quad (25)$$

where $P(R)$ is the size distribution function. A major contribution in the interpretation of experimental data is that if the size distribution is too broad, a given transition (ij) for size R_1 could overlap with another transition $(i'j')$ for size R_2 .

III. RESULTS

A. Single Particle States

Using the Hamiltonian described in Section II A, the 48 highest energy hole states and the 24 lowest energy electron states were calculated for the InAs dots listed in Table III. Figure 5 shows plots of the electron and hole wavefunctions squared, for the dot with a diameter of 42.2Å, in a plane through the center of the dots. The plots show that as a result of the large band offsets between the vacuum and the InAs dot, the wavefunctions are strongly localized within the InAs dot. Approximately 90.5% and 95.9% of the ground state electron and hole wave function squared respectively, are localized within the dot.

The single-particle energies of the highest energy hole state and the lowest energy electron state are plotted as a function of diameter in Fig. 6. For comparison, the same states obtained from a recent Wannier function based, *single-band* pseudopotential calculation of Mizel and Cohen [15] are also shown. Figure 6 shows that in both calculations, as the size of the InAs dot increases, the quantum confinement decreases, such that the VBM and CBM approach the bulk VBM and CBM values. We have fitted the size dependence of the dot VBM and CBM according to

$$\begin{aligned}\epsilon_{vbm}^{dot} &= E_{vbm}^{bulk} + \frac{a}{R^{n_v}} \\ \epsilon_{cbm}^{dot} &= E_{cbm}^{bulk} + \frac{b}{R^{n_c}} \quad ,\end{aligned}\quad (26)$$

where R is the radius of the InAs dot. This fitting reveals that the size exponents, $n_{v,c}$, of the hole and electron quantum confinements are significantly different to the effective mass exponents:

$$n_v = \begin{cases} 1.21 & \text{Current Pseudopotential} \\ 1.59 & \text{Single band [15]} \\ 2.0 & \text{EMA} \end{cases} \quad n_c = \begin{cases} 0.95 & \text{Current Pseudopotential} \\ 1.23 & \text{Single band [15]} \\ 2.0 & \text{EMA} \end{cases} . \quad (27)$$

Figure 6 also shows that while the CBM states calculated with the multi-band pseudopotential and the single-band method are almost identical in energy, the VBM states calculated

using the single-band method are higher in energy than those calculated using the pseudopotential. This difference can be attributed to the fact that the real dot valence band has strong interband coupling, so the single band approximation used by Mizel and Cohen [15] is more severe for the valence band. For the CBM states, the single band approximation is sufficient because the energy spacing between bands is large and there is therefore little interband coupling.

Single Particle Gaps: In Fig. 7(a) we plot the single particle band gaps obtained from our multi-band pseudopotential calculations. For comparison we also show the single particle gaps obtained from the single band calculations [15] of Mizel and Cohen and the 8 band k.p calculations from Ref [32]. Figure 7(a) shows that the single band calculations [15] tend to underestimate the single particle gap with respect to the more converged calculations, as a result of the underestimate of the valence band quantum confinement in single band models. The 8 band k.p and current multi-band pseudopotential results show good agreement with each other. In Fig. 7(b) we compare the multi-band pseudopotential calculations with a recent PL experiment, by extracting the single particle gaps from experimental results from Ref. [6] by subtracting an approximate value for the electron-hole Coulomb energy calculated from $E_{coul} = 3.572/2\epsilon R$ (Ref. [30]). Here ϵ is the static dielectric constant of bulk InAs and R is the dot radius in atomic units. We also show the results of the single-particle gap extracted from a new STM tunnelling experiment [33] on the same colloidal InAs dots. The multi-band pseudopotential calculations predict larger gaps than those measured by PL. This can have three reasons (i) the observed emission could involve surface states below the CBM and above the VBM and would therefore have a lower energy than the calculated band to band values. (ii) The calculation assumes a single dot, while in the experiment there is an ensemble of dots. Thus, the observed emission could be of low energy since the largest dots in the ensemble, having the lowest CBM and highest VBM energies emit. In addition (3) measured sizes suffer from the notorious difficulty of measuring size accurately. If the measured TEM size is underestimated, (especially for the samll dots) this could explain the discrepancy. The new tunellling STM experiments on similar InAs dots, Banin *et. al.*

measure a single particle gap that is higher than that extracted from the optical experiment and is in much better agreement with the calculations.

We fit the single particle (sp) band gap to the following power law,

$$E_{sp}^{dot} = E_{sp}^{bulk} + AD^n \quad , \quad (28)$$

taking the bulk gap as 0.42 eV. Our pseudopotential results yield a size exponent $n_{sp} = -1.01$. This is considerably smaller than the effective mass predicted value of -2. In the previous section we have seen that the Coulomb interaction J_{ij} scales as $R^{-1.8}$, while here we see that the single particle gap scales as $R^{-1.01}$. Thus the *relative* importance of Coulomb effects increases for small dots. This is the opposite of the effect predicted by single-band effective mass predictions of $J(R) \sim R^{-1}$ and $E_{gap} \sim R^{-2}$. The scaling, n , of the single particle band gap is compared with similar calculations for InP, CdSe and Si dots in Table IV.

Excitonic gaps: In Fig. 7(c) we plot the actual PL results along with our multi-band pseudopotential excitonic results calculated from Eq.(12) including the electron-hole Coulomb energy screened according to Eq.(13). The single-particle pseudopotential results from Fig. 7(a) are shown for comparison. The size exponent for the excitonic gap is $n_{exciton} = -0.90$, smaller than that for the single particle gap ($n_{sp} = -1.01$). Using the Coulomb energy from Eq.(13) rather than Eq.(22) improves the agreement with experiment in Fig. 7(b) by a factor of 3. However, the fit is still not particularly good. The reasons for this were discussed above.

Confinement energies: We have also calculated the ratio of the conduction band quantum confinement, $\Delta E_{CB}(R)$, to the valence band quantum confinement, $\Delta E_{VB}(R)$, defined as

$$\begin{aligned} \Delta E_{CB}(R) &= \epsilon_{cbm}^{dot} - \epsilon_{cbm}^{bulk} \\ \Delta E_{VB}(R) &= \epsilon_{vbm}^{dot} - \epsilon_{vbm}^{bulk} \quad . \end{aligned} \quad (29)$$

Define $\xi(R)$ as

$$\xi(R) = \frac{\Delta E_{CB}(R)}{\Delta E_{VB}(R)} \quad (30)$$

Our multi-band calculations for InAs dots find a value of $\xi(R)$ that decreases with R . The

best linear fit (constant $\xi(R)$) to the data yields a ratio, $\xi(R)$, of 3.13 for the multiband calculations. For Si dots, $\xi(R)$ was recently measured [34] to have a value of 0.5.

Within the single-band effective mass approximation, assuming an infinite potential barrier at the surface, the quantum confinement of electrons and holes can be written as $\Delta\epsilon_{e,h} = \hbar^2\pi^2/2m_{e,h}^*R^2$, where $m_{e,h}^*$ is the effective mass of electrons and holes at the Γ point and R is the size of the quantum dot. The ratio of electron confinement to hole confinement

$$\xi(R) = \frac{\Delta E_{cbm}(R)}{\Delta E_{vbm}(R)} = \frac{m_h^*}{m_e^*} = \text{const.} \quad (31)$$

is therefore given by the ratio of the electron and hole effective masses which is approximately 15.4. This is significantly different to our multiband calculated value of 3.13. This difference can be attributed to the fact that the pseudopotential calculated hole states are derived from a mixture of the bulk heavy and light hole states.

B. The nature of the single particle wavefunctions

The results of the single particle wavefunction analysis from Eqs.(8)-(10) is given for the 42.2Å diameter dot in Table V. Details of the analysis for the other dot sizes are given at Ref. [35]. Only the states which contribute to the excitonic peaks discussed in Section II C are listed in the table. For each state, the fraction of the wavefunction derived from the bulk Γ -like split off, heavy (Γ_{8v}) and light hole (Γ_{7v}) and lowest conduction band (Γ_{6c}) states is given (see Fig. 1). For each of these bulk states, the fraction of the total wavefunction derived from envelope functions with s , p and d symmetry is also given. The significant contributions to each state are marked in bold. Contributions less than 0.01 have been set to zero. For example, the highest energy hole state has a fraction of $0.0 + 0.02 + 0.02 = 0.04$ derived the bulk split-off band, $0.50 + 0.29 + 0.09 = 0.89$ derived from the bulk heavy and light hole bands and $0.0 + 0.02 + 0.0 = 0.02$ derived from the lowest bulk conduction band. The remaining 0.05 fraction is derived from bulk bands further from the band gap, and from higher angular momentum envelope functions.

Analysis of the results in Table V and those for the other size dots reveals several interesting properties of the single particle wavefunctions:

- (1) The origin of the lowest lying electron states in the dot follows qualitatively the predictions of single band effective mass theory. For example, the lowest electron state of the 42.2Å diameter dot (see Table V) is 69% derived from the bulk conduction band edge state (Γ_{6c}) with an *s*-like envelope function. The next two highest electron levels are 64% derived from the same bulk Bloch state, but with a *p*-like envelope functions.
- (2) As a result of the small band gap of bulk InAs, there is a strong coupling between the electron and hole states. Approximately 20% of the weight of the lowest energy *electron states* in the dot is derived from the split-off, heavy and light hole ($\Gamma_{8v} + \Gamma_{7v}$) bulk states. This valence-conduction mixing explains why the 6x6 k.p method, which ignores such coupling, fails to describe these states in InAs dots.
- (3) The highest energy hole states in the dot have significant weight from both the *s* and *p* envelope functions from both heavy and light hole bulk states. They therefore cannot be described, even qualitatively, by a single band model. The VBM of the 42.2Å diameter dot (see Table V) has 50% *s* and 29% *p* character. Similarly, the lowest electron state in the dot has 27% non-*s* character, originating from valence bands. Such an *s-p* mixing is largely absent in current theoretical descriptions of InAs dots via the k.p method [11].
- (4) The order of the electron and hole states changes with size. This reflects different size scaling of the quantum confinement for different states. For example in the 42.2Å diameter dot (see Table V) the lowest conduction state is *s*-like (69%), then states 2,3 and 4 are *p*-like (64%), then states 5,6,7 and 8 (not shown in the table) are a mixture of *d* and *g*. In the 30.3Å diameter dot, the states with 42% *p* character have moved above the states identified by their significant *d* and *g* character making them states 6,7 and 8 as opposed to 2,3 and 4. Similarly, in the valence band the state with 37% *s*-like contribution from the split off band and 13% and 12% from *p* and *d* envelopes of heavy and light hole states is the 5th and 6th state from the top of the valence band in the 30.3Å diameter dot but moves to the 11th and 12th state from the top of the valence band in the 42.2Å diameter dot.

C. Calculated Single-dot absorption spectra

Theoretical single-dot absorption spectra were calculated for each of the dots listed in Table III using the method described in section II C. These spectra are shown in Figs. 8(a)-(d). The identities of each of the major peaks in the spectra were determined by examining the nature of the initial and final single particle states contributing to each peak. The following criteria were used to establish these identities.

1. The ratio of the contributions to the single particle states from the heavy hole, light hole, split off and conduction states.
2. The contribution of each angular momentum component from the heavy hole, light hole, split off and conduction states.
3. The total angular momentum, F , of each single particle state (see section II B).
4. The strength of the dipole transition probability matrix element for each peak.

Table VI shows the identities of the peaks for the 42.2Å diameter dot. Details of the analysis for the other dot sizes are given at Ref. [35]. They show that there are two separate manifolds of transitions: peaks (a) to (e) which correspond to transitions from the dot hole states to the *lowest s*-like electron state and peaks (f) to (k) which correspond to transitions from the dot hole states to the *next highest p*-like electron state. The analysis of the peaks shows:

(a) “peak a” represents the fundamental band gap transition. The initial valence state associated with this peak is a doubly degenerate hole state with s and p character derived from both heavy and light hole bulk states. This initial state has a total angular momentum, F , that ranges from 1.75 to 2.01. The final conduction state is the singly degenerate, lowest energy electron state, with an s -like envelope function and a total angular momentum that ranges from 1.11 to 1.27. In the approximate k.p language, this transition is closest to the $S_{3/2}$ to $S_{1/2}$ transition.

(b) “peak b” corresponds to a transition with very weak intensity. For the largest dot with 42.2Å diameter, this state has merged with peak (a) and cannot be resolved. The initial

valence state associated with this peak is a doubly degenerate hole state with p character derived from both heavy and light hole bulk states. It is the second highest energy hole state. This initial state has a total angular momentum that ranges from 1.92 to 2.51. The final conduction state is the same as in peak (a). In the approximate k.p language this transition is closest to the $P_{5/2}$ to $S_{1/2}$ transition.

(c) “peak c” has a strong intensity. The initial valence state associated with this peak is a doubly degenerate hole state with a mix of s , p and d character. Its most significant contribution is from the split-off state but it contains some heavy and light hole character. This initial state has a total angular momentum that ranges from 1.99 to 2.48. The final conduction state is the same as in peak (a). In the approximate k.p language this transition is closest to the $P_{5/2}$ to $S_{1/2}$ transition.

(d) “peak d” is a transition with very weak intensity. For the largest dot with 42.2Å diameter this transition merges with “peak c” and is no longer distinguishable. The initial valence state associated with this peak is a doubly degenerate hole states with a mix of mostly s and d character. It is derived from the bulk heavy and light hole states. This initial state has a total angular momentum that ranges from 2.48 to 3.25. The final conduction state is the same as in peak (a). In the approximate k.p language this transition is closest to the $S_{5/2}$ to $S_{1/2}$ transition.

(e) “peak e” has a similar origin to “peak d” and also has a very weak intensity. It also merges with “peak c” in the largest dot with 42.2Å diameter. The initial valence state associated with this peak is a singly degenerate hole state with a mix of s , d and some g character. It is derived from both the bulk spin-orbit, heavy and light hole states. This initial state has a total angular momentum that ranges from 3.03 to 3.75. The final conduction state is the same as in peak (a). In the approximate k.p language this transitions is closest to the $S_{7/2}$ to $S_{1/2}$ transition.

(f) “peak f” corresponds to a transition with very weak intensity that is only observed in the two smaller dots. It has the same initial state as “peak a”, but the final state is the next highest conduction state. This conduction state is a triply degenerate state, with a

p -like envelope function and a total angular momentum that ranges from 2.15 to 2.19. In the approximate k.p language, this transitions is closest to the $S_{3/2}$ to $P_{3/2}$ transition.

(g) “peak g” corresponds to a transition from the same initial state as “peak b”, to the p -like conduction state. This is a very intense peak that is observed in all the sizes of dot. In the approximate k.p language, this transitions is closest to the $P_{5/2}$ to $P_{3/2}$ transition.

(h) “peak h” is also a very intense peak that is observed in all the sizes of dot. The initial valence states are a combination of the same initial state as “peak c” and also a doubly degenerate hole state, very close in energy to this state with mostly s and f character, derived from heavy and light hole states, with a total angular momentum ranging from 2.66 to 2.72. The final conduction state is the same as in peak (f). In the approximate k.p language, this transition is closest to the $P_{5/2}$ to $P_{3/2}$ transition. It is possible that the proximity of peaks (g) and (h) combined with their strong intensity would not allow them to be distinguished in a photoluminescence experiment. This is discussed further in section III E.

(i) “peak i” is has a weaker intensity, but is observed in all the sizes of dot. The initial valence state is the same as “peak d”. The final conduction state is the same as in peak (f). In the approximate k.p language, this transition is closest to the $S_{5/2}$ to $P_{3/2}$ transition. This transition is weakly allowed.

(j) “peak j” corresponds to a transition with strong intensity. The initial valence state associated with this peak is a doubly degenerate hole state containing mostly a mix of p , d and f character. Its contains significant contributions from both the bulk split-off state and the heavy and light hole states. This initial state has a total angular momentum that ranges from 3.03 to 3.41. The final conduction state is the same as in peak (f). In the approximate k.p language, this transition is closest to the $S_{7/2}$ to $P_{3/2}$ transition.

(k) “peak k” corresponds to a transition with weak intensity. The initial valence state associated with this peak is a doubly degenerate hole state containing mostly p character. It is mostly derived from the bulk heavy and light hole states. This initial state has a total angular momentum that ranges from 3.19 to 3.24. The final conduction state is the same

as in peak (f). In the approximate k.p language, this transition is closest to the $P_{7/2}$ to $P_{3/2}$ transition.

Having discussed the identities of the peaks in each dot size, we next wish to see how to connect peaks with the same identities in different sizes of dot. This is not always possible, as different sizes of dot might have some peaks that are fundamentally new, or two peaks that have merged together. We have labelled in Fig. 8 and in Table VI the peaks that originate from similar excitons in the different sizes of dot by the same letters (a) to (k).

D. Comparison of calculated single-dot spectra with the experimental absorption spectra

The positions of the above peaks are plotted as a function of diameter for each dot in Fig. 9 and with respect to the band gap of each dot in Fig. 10. As some of the peaks merge with each other in the larger dots, not all the peaks are marked for all the sizes of dot. The predictions of Figs. 9 and 10 pertain to hypothetical samples each containing dots of a single size and spherical shape. The actual synthesized samples [11] contain a significant, but unknown, distribution of dot sizes and shapes. Nevertheless, the experimental results from Ref. [11] are included in Figs. 9 and 10. It should be noted that where two peaks have effectively merged together, or where the weight of a particular peak is too small to be detected (e.g. peak “b”), these points are not plotted in Figs. 9 and 10. A comparison of the pseudopotential results in Fig. 10 with the results from Ref. [11] is given in Table VII, which shows that

1. Peak (a), by definition, corresponds to the experimentally measured band gap, E1.
2. We ascribe two weak sets of peaks (c and d) as originating from the weakly observed E2 experimental peak.
3. For the E3 peak we calculate a single peak (e).
4. For the weakly observed E4 peak we find no calculated counterpart.

5. The strongest two calculated peaks (g and h) fall on either side of the E5 peak and it is possible that the strength of these excitations could prevent them from being isolated in the experiment. They are also merged by a finite size distribution (see section III E).
6. The final two calculated peaks (j and k) correspond to the experimental E6 and E7 data.

For each of the peaks, the calculated scaling of the exciton energy *spacings* with dot size (or band gap) shows reasonable agreement with the experimental results. However, Fig. 9 shows that the calculated values of the *absolute* exciton peaks appears to exhibit a different size dependence to that observed in Ref. [11]. This lack of agreement can be attributed in part to the finite size and shape distribution present in the experimental samples. This is discussed in the following section.

E. Ensemble absorption spectra

The ideal comparison between theory and experiment is between the calculated (Fig. 8) and measured *single-dot* spectra. However, no such single-dot measurements currently exist for InAs quantum dots. Our predicted single-dot spectra for different sizes (Fig. 8) suggest that the interpretation of an ensemble spectra could differ qualitatively from the interpretation of a single dot spectra. This calls for measurement of the single dot spectra. For example, peak (b) in the dot with a diameter of 30.3 Å coincides with peak (e) in the dot with a diameter of 36.9 Å and with peak (g) in the dot with a diameter of 42.2 Å. Thus, if the experimentally accessible samples represent a broad size distribution it is impossible to ascribe consistently experimental peaks to unique calculated single-dot peaks.

We try to quantify the effect of a finite size distribution in the experimental samples by using our single dot spectra in combination with Eq.(24) to calculate *ensemble* absorption spectra. These are not directly comparable with the size selected PLE results from Ref. [6], but are designed to provide a general indication of the effects of size distribution on

the absorption spectra of an ensemble of dots. We neglect shape distribution effects, since they are not quantified experimentally. Transmission electron microscopy studies of III-V semiconductor quantum dots [36] show that there are two factors producing an ensemble of different dot volumes. Firstly, in any sample there is a finite range of dot diameters. Secondly, the dots are ellipsoidal in shape, with a range of ratio of major to minor axes. We have therefore chosen to model the distribution of sizes, $P(R)$, in Eq.(24) by a simple Gaussian, whose width, σ_R , builds in the size distribution,

$$P(R) = \frac{1}{\sqrt{2\pi}\sigma_R} e^{-(R-R_0)^2/2\sigma_R^2} . \quad (32)$$

In Fig. 11(a) we plot ensemble absorption spectra calculated from Eq.(24) for quantum dots with a mean diameter of 23.9 Å and standard deviations, σ_R , of 0, 5 and 10% of the mean size. The function $I(E, R)$ in Eq.(24) was obtained by fitting the size dependence of each of the peaks, i , in Fig. 9 to $E_i(R) = E_i^0 + aR^N$ and then summing the contributions from all the peaks so that

$$I(E, R) = \sum_{peaks,i} \alpha_i e^{-(E-E_i(R))^2/2\sigma_0^2} , \quad (33)$$

where α_i is the relative intensity of peak i , and σ_0 is the intrinsic line width of the peaks, set to 5 meV. Figures 11(b) to (d) show similar ensemble absorption spectra for dots with size distributions that have mean diameters of 30.3, 36.9 and 42.2 Å and standard deviations of 5%. Figures 11(a) to (d) show that as the width of the size distribution increases, the peaks become “smeared out”. With a standard deviation of 5% it is still possible to resolve peaks, (a), (c), (g) and (h). However, peak (j) is just a small shoulder on peak (h). With a standard deviation of 10% peaks (g) and (h) have effectively merged together. The merging effect becomes more severe as the mean size of the dots increases as the initial spacing of the peaks is smaller for larger dots.

Figure 12 shows how the centers of the broadened peaks in each of the 5% ensemble spectra from Fig. 11 vary with size. Figure 12 is the size ensemble equivalent of the single dot results plotted in Fig. 10. As in Fig. 10, the experimental results of Banin *et. al.* are plotted for comparison. Comparison of Figs. 10 and 12, reveals that

1. The fundamental transition (a) is still clearly resolvable in the ensemble spectra and corresponds to experimental peak E_1 .
2. The first excited state (c) is still clearly resolvable in all sizes of dot. This peak probably still corresponds to peak E_2 .
3. Peak (d) is only resolvable in the two smallest dots, where it is close to the experimental E_3 peak.
4. For the larger two dots, peaks (g) and (h) merge to form one large peak. The position of this merged peak is close to the experimental E_5 peak. For the two smaller dots, the peak splits into two peaks (g) and (h) with different size scaling behaviour.
5. Peak (j) is only resolvable from peaks (g) and (h) in the two smaller dots, where it could correspond to either the experimental E_6 or E_7 peaks.
6. The weaker peaks (b), (e) and (k) are not individually resolvable for any size of dot in the ensemble spectra.

IV. CONCLUSIONS

We have performed pseudopotential calculations for the electronic structure of both the ground and excited states of free standing InAs quantum dots for a range of experimentally realistic sizes. Using calculated electron-hole Coulomb energies and dipole matrix transition probabilities we have constructed single-dot absorption spectra for 4 different sizes of quantum dot. These spectra exhibit a series of clearly resolvable exciton peaks. The size dependence of the spacing between the exciton peaks in these single dot spectra shows partial agreement with those found in recent experiments. By fitting the size dependence of each exciton peak and postulating a Gaussian distribution of dot sizes, we have calculated ensemble absorption spectra. The size scaling of the peaks in these ensemble spectra shows a better agreement with the experimental data.

We also have analyzed the single particle parentage of each excitonic peak. We find that (i) as a result of the small band gap of InAs, there is significant valence-conduction band mixing in the quantum dot states, (ii) the removal of spherical symmetry of these dots produces odd-even mixing in these states.

Our predicted single-dot excitonic spectra (Fig. 8) await experimental testing. Our predicted ensemble spectra (Figs. 11) are not in as good agreement with experiment as our results for InP [13] and CdSe [12] dots. Sample quality, including shape distributions could be a factor in this relative lack of agreement.

Acknowledgements We thank L.W. Wang and A. Franceschetti for useful discussions and their comments on the manuscript. This work was supported DOE – Basic Energy Sciences, Division of Materials Science under contract No. DE-AC36-98-GO10337.

REFERENCES

- [1] A. Zunger, MRS Bulletin **23**, 35 (1998).
- [2] N. Carlsson, W. Seifert, A. Petersson, P. Castrillo, M.E. Pistol and L. Samuelson, Appl. Phys. Lett **66**, 3093 (1994).
- [3] K. Schmidt, G. Medeiros-Ribeiro, M. Oestreich, and P. Petroff, Phys. Rev B. **54**, 11346 (1996).
- [4] M. Grundmann, O. Stier, and D. Bimberg, Phys. Rev. B **52**, 11969 (1995).
- [5] S. Empedocles, D. Norris, and M. Bawendi, Phys. Rev. Lett. **77**, 3873 (1996).
- [6] A. Guzelian, U. Banin, A. Kadavanich, X. Peng, and A. Alivisatos, Appl. Phys. Lett. **69**, 1432 (1996).
- [7] O. Micic, J. Sprague, Z. Lu, and A. Nozik, Appl. Phys. Lett. **68**, 3150 (1996).
- [8] D. Norris and M. Bawendi, Phys. Rev. B **53**, 16338 (1996).
- [9] A. Colvin, V.L. and Alivisatos and J. Tobin, Phys. Rev. Lett. **66**, 2786 (1991).
- [10] D. Bertram, O. Micic, and A. Nozik, Phys. Rev. B **57**, R4265 (1998).
- [11] U. Banin, J.C. Lee, A.A. Guzelian, V. Kadavanich, A.P. Alivisatos, W. Jaskolski, G.Q. Bryant, Al.L. Efros and M. Rosen J. Chem. Phys. **109**, 2306.
- [12] L.-W. Wang and A. Zunger, J. Phys. Chem. **102**, 6449 (1998).
- [13] H. Fu and A. Zunger, Phys. Rev. B **57**, R15064 (1998).
- [14] L.-W. Wang and A. Zunger, Phys. Rev B. **53**, 9579 (1996).
- [15] A. Mizel and M. Cohen, Solid State Commun. **104**, 401 (1998).
- [16] S. Zhang and A. Zunger, Phys. Rev. B **48**, 11204 (1993).
- [17] A. Williamson and A. Zunger, Phys. Rev. B **58**, 6724 (1998).

[18] J. Kim, L.-W. Wang, and A. Zunger, Phys. Rev. B **57**, R9408 (1998).

[19] A. Williamson and A. Zunger, Phys. Rev. B , Code: BU6515 (1998).

[20] L.-W. Wang, J. Kim, and A. Zunger, Phys. Rev B. **59**, 5678 (1999).

[21] In practice, we use two artificial barrier materials, one for valence band calculations, and one for the conduction band. The use of two separate potentials enables us to achieve larger valence and conduction band offsets (VBO and CBO), between the dot and the barrier, than could be realized with a single artificial barrier material. We have a VBO of 2.1 eV and a CBO of 3.2 eV. The fitted values for the artificial barrier are given in Table II Although, in principle, the choice of different barrier potentials means the valence and conduction states are no longer orthogonal, in practice the difference in the barrier potentials is small and there is also minimal spillage of the wavefunctions into this barrier material. The resulting overlap between valence and conduction states is typically only 3×10^{-5} .

[22] L.-W. Wang and A. Zunger, Phys. Rev B. **51**, 17398 (1995).

[23] L.-W. Wang and A. Zunger, J. Chem. Phys. **100**, 2394 (1994).

[24] L.-W. Wang and A. Zunger, *Semiconductor Nanoclusters*, Elsevier Science, Amsterdam, 1996.

[25] A. Franceschetti, H. Fu, L.-W. Wang, and A. Zunger, Phys. Rev. B. **60**, 1819 (1999).

[26] R. Resta, Phys. Rev. B **16**, 2717 (1977).

[27] H. Haken, Nuovo Cimento **10**, 1230 (1956).

[28] R. Tsu, L. Ioriatti, J. Harvey, H. Shen, and R. Lux, Mater. Res. Soc. Symp. Proc. **283**, 437 (1993).

[29] D. Penn, Phys. Rev **128**, 2093 (1962).

[30] L. Brus, J. Phys. Chem. **90**, 2555 (1986).

[31] A. Franceschetti and A. Zunger, Phys. Rev. Lett. **78**, 915 (1997).

[32] U. Banin, C.J. Lee, A.A Guzelian, A.V. Kadavanich, A.P. Alivisatos, W. Jaskolski, G.W. Bryant, Al.L. Efros and M. Rosen J. Chem. Phys. **109**, 2306 (1998).

[33] U. Banin, D. Katz, and O. Millo, Nature , accepted for publication (1999).

[34] T. van Buuren, L. Dinh, L. Chase, W. Siekhaus, and L. Terminello, Phys. Rev. Lett. **80**, 3803 (1998).

[35] More details can be found in the “downloadable data” section of <http://www.sst.nrel.gov>.

[36] O. Micic, H.M. Cheong, H. Fu, A. Zunger, J.R. Sprague, A. Mascarenhas and A.J. Nozik J. Phys. Chem. B **101**, 4904 (1997).

[37] Landolt and Borstein, *Numerical Data and Functional Relationships in Science and Technology, Volume 22, Subvolume a*, Springer-Verlag, Berlin, 1997.

[38] H. Fu and A. Zunger, Phys. Rev. B **55**, 1642 (1997).

[39] F.Reboreda and A. Zunger, Phys. Rev. B , BE7134.

TABLES

TABLE I. Experimental and fitted bulk InAs pseudopotential properties. Δ_{SO} is the spin-orbit splitting and $m_{\Gamma_{1c}}^*$, $m_{\Gamma_{15v},hh}^*$ and $m_{\Gamma_{15v},lh}^*$ are the effective masses of electrons, heavy and light holes.

Property	Expt. Value [37]	Pseudopotential
$\Gamma_{1c} - \Gamma_{15v}$ (eV)	0.42	0.41
$X_{1c} - \Gamma_{15v}$ (eV)	2.33	2.27
$L_{1c} - \Gamma_{15v}$ (eV)	1.71	1.61
Δ_0 (eV)	0.38	0.36
$m_{\Gamma_{1c}}^*$	0.029	0.028
$m_{\Gamma_{15v},hh}^*[100]$	0.43	0.41
$m_{\Gamma_{15v},lh}^*[100]$	0.038	0.039

TABLE II. Screened atomic pseudopotential parameters for InAs and the barrier potentials.

The a parameters refer to Eq.(2).

	a_0	a_1	a_2	a_3
In	118.781	1.783	3.382	0.393
Barrier Cation (cond)	107.755	1.915	3.460	0.414
Barrier Cation (val)	333.070	0.120	3.126	0.521
As	65.943	2.664	1.684	0.637
Barrier Anion (cond)	19.892	2.097	1.182	0.243
Barrier Anion (val)	49.614	2.737	1.523	0.574

TABLE III. InAs quantum dot sizes and compositions

Dot Number	1	2	3	4
No. In atoms	140	276	456	736
No. As atoms	141	249	459	683
Diameter (Å)	23.9	30.3	36.6	42.2

TABLE IV. A comparison of the size scaling exponent, n , in R^{-n} of the unscreened electron-hole Coulomb energy, ϵJ , the screened electron-hole Coulomb energy, J , the single particle band gap, E_{gap}^{sp} and the excitonic band gap $E_{gap}^{exciton}$ [Eq.(12)] for InAs, InP, CdSe and Si quantum dots.

Property	InAs	InP [38]	CdSe [12]	Si [39]	EMA
ϵJ	0.70		0.86	0.82	1
J	1.79	1.35	1.18	1.50	1
E_{gap}^{sp}	1.01	1.16	1.64	1.20	2
$E_{gap}^{exciton}$	0.90	1.09	1.93	1.18	

TABLE V. Contributions (as fractions of unity) from the split-off (SO), heavy hole (hh), light hole (lh) and conduction band (CBM) bulk states to the single particle states of the InAs dot with 42.2Å diameter. The dot states are numbered (first column) from the band edge. For electron states 1 is the lowest in energy, 8 the highest. For hole states, 1 is the highest in energy, 24 the lowest. The contribution from each state is determined using Eq.(8). For each state the bulk SO, hh+lh and CBM contributions are decomposed into their angular momentum components using Eq.(10). Only the states contributing to the major excitonic peaks in Fig. 8 are shown. All entries less than 0.01 are set to 0.0. The main contributions are marked in bold. Totals include envelope functions with angular momenta from 0 to 6.

Level	Energy (eV)	SO Contribution				hh + lh Contribution				CBM Contribution			
		<i>s</i>	<i>p</i>	<i>d</i>	Total	<i>s</i>	<i>p</i>	<i>d</i>	Total	<i>s</i>	<i>p</i>	<i>d</i>	Total
Conduction States													
1	ϵ_c	0.	0.07	0.	0.07	0.	0.20	0.	0.20	0.69	0.	0.	0.69
2	$\epsilon_c + 0.360$	0.06	0.	0.01	0.07	0.01	0.	0.19	0.20	0.	0.64	0.01	0.65
3,4	$\epsilon_c + 0.361$	0.	0.	0.07	0.07	0.09	0.	0.10	0.19	0.	0.64	0.01	0.65
Valence States													
1,2	ϵ_v	0.	0.02	0.02	0.04	0.50	0.29	0.09	0.89	0.	0.02	0.	0.02
3,4	$\epsilon_v - 0.014$	0.	0.01	0.01	0.03	0.23	0.55	0.07	0.88	0.	0.01	0.	0.01
7,8	$\epsilon_v - 0.098$	0.	0.02	0.02	0.08	0.08	0.38	0.18	0.78	0.	0.	0.02	0.02
11,12	$\epsilon_v - 0.123$	0.28	0.	0.	0.31	0.	0.26	0.19	0.56	0.	0.	0.01	0.01
13	$\epsilon_v - 0.140$	0.	0.21	0.06	0.28	0.	0.12	0.21	0.60	0.	0.	0.	0.
15,16	$\epsilon_v - 0.175$	0.	0.06	0.01	0.14	0.02	0.26	0.05	0.73	0.	0.	0.	0.
18	$\epsilon_v - 0.189$	0.	0.04	0.13	0.27	0.07	0.16	0.04	0.69	0.	0.	0.	0.
23,24	$\epsilon_v - 0.223$	0.	0.05	0.01	0.14	0.01	0.33	0.12	0.69	0.	0.	0.02	0.02

TABLE VI. Analysis of the significant absorption peaks for a dot with 42.2Å diameter. The peak letters refer to the labelling of the peaks in Figs. 10 and 8. Peak energies are calculated according to Eq.(12). The valence and conduction indices refer to the number of the state from the band edge (i.e. VBM and CBM have index 1 etc). The envelope function information summarizes the results from Table V. Note, the notation “s”, “p” etc refers to the orbital content of the wavefunctions, not the specific number of nodes. All energies are in eV.

Peak	Peak Energy	Initial valence state				Final conduction state			
		Index	Energy	Envelope	F	Index	Energy	Envelope	F
(a)	1.209	1,2	-5.8260	<i>s</i> + <i>p</i>	1.77	1	-4.516	<i>s</i>	1.11
(c)	1.335	11,12	-5.9491	<i>p</i> + <i>d</i>	2.48	1	-4.516	<i>s</i>	1.11
(g)	1.588	3,4	-5.8401	<i>p</i>	1.90	2,3,4	-4.156	<i>p</i>	1.92
(h)	1.675	7,8	-5.9240	<i>s</i> + <i>p</i> + <i>f</i>	2.66	2,3,4	-4.156	<i>p</i>	1.92
(i)	1.717	13	-5.9660	<i>p</i> + <i>d</i> + <i>f</i>	2.93	2,3,4	-4.156	<i>p</i>	1.92
(j)	1.760	15,16	-6.0087	<i>p</i> + <i>f</i>	3.07	2,3,4	-4.156	<i>p</i>	1.92
(k)	1.800	23,24	-6.0491	<i>p</i>	3.19	2,3,4	-4.156	<i>p</i>	1.92

TABLE VII. Comparison of the current multi-band pseudopotential assignment and the k.p assignment from Ref. [11] of the experimentally observed optical transitions in Ref. [11]. The initial states and final states of each transition are denoted by nQ_F , where n is the principal quantum number, Q the lowest angular momentum component of the wavefunction and F total angular momentum. Note, it is only possible to determine the envelope function angular momentum and total angular momentum for the multi-band pseudopotential wavefunctions.

Peak	Pseudopotential assignment	Closest Expt. Peak	k.p assignment
		from Ref. [11]	from Ref. [11]
(a)	$S_{3/2} \rightarrow S_{1/2}$	E ₁	$2S_{3/2} \rightarrow 1S_{1/2}$
(b)	$P_{5/2} \rightarrow S_{1/2}$	Not observed	No prediction
(c)	$P_{5/2} \rightarrow S_{1/2}$	E ₂ /E ₃	No prediction
(d)	$S_{5/2} \rightarrow S_{1/2}$	E ₂	No prediction
(e)	$S_{7/2} \rightarrow S_{1/2}$	E ₃	$2S_{3/2} \rightarrow 1S_{1/2}$
(g) and (h)	$P_{5/2} \rightarrow P_{3/2}$	E ₅	$1P_{3/2} \rightarrow 1P_{3/2}$ $1P_{3/2} \rightarrow 1P_{1/2}$
(j)	$S_{7/2} \rightarrow P_{3/2}$	E ₆	$2S_{1/2} \rightarrow 1S_{1/2}$
(k)	$P_{7/2} \rightarrow P_{3/2}$	E ₇	$1P_{1/2} \rightarrow 1P_{3/2}$ $1P_{1/2} \rightarrow 1P_{1/2}$

FIGURES

FIG. 1. InAs bulk band structure from the L to Γ to X calculated with the empirical pseudopotential defined in Eq.(2).

FIG. 2. The electronic and ionic contributions to the dielectric screening function. Plotted in reciprocal space.

FIG. 3. The screened dielectric function. Plotted in real space for each of the 4 InAs dots given in Table III.

FIG. 4. Electron-hole Coulomb energies calculated using both pseudopotential [Eq.(13)] and effective mass [Eq.(22)] expressions for all 4 sizes of InAs quantum dot given in Table III.

FIG. 5. Highest energy hole and lowest energy electron wavefunctions squared in a plane through the center of the dot for a free standing spherical InAs quantum dot with diameter of 42.2 Å.

FIG. 6. Size dependence of the lowest energy hole state and highest energy electron states, calculated using the present multi-band pseudopotential and single band techniques. The circles and triangles mark the present multi-band pseudopotential and single band (Wannier function) results. The solid lines are the best fit to a scaling of $E_0 + AR^n$ (see Eq.(26)).

FIG. 7. (a) Calculated single particle band gaps calculated using present multi-band pseudopotential (circles), 8x8 k.p (solid line) and single band techniques (squares). (b) Measured single particle band gaps using Photoluminescence (solid line) and STM experiments (triangles). (c) Present multi-band pseudopotential results (circles) including the electron-hole Coulomb energy calculated from Eq.(13) vs PL data.

FIG. 8. Calculated absorption spectra for single InAs quantum dots with diameters of (a) 23.9, (b) 30.3, (c) 36.6 and (d) 42.2 Å. The labels (a)-(k) refer to the classification of the states in Table VI.

FIG. 9. Pseudopotential calculated (circles) absolute positions of absorption peaks *vs* $1/R^2$ for InAs quantum dots with diameters 23.9, 30.3, 36.6 and 42.2Å. The pseudopotential results are connected using the analysis from section III C. Experimental results from Ref. [11] are represented by the black lines.

FIG. 10. Pseudopotential calculated (circles) positions of absorption peaks minus the band gap *vs* band gap for InAs quantum dots with diameters 23.9, 30.3, 36.6 and 42.2Å. The pseudopotential results are connected using the analysis from section III C. The labels (a)-(k) refer to the classification of the states in Table VI. Experimental results from Ref. [11] are represented by the black symbols and lines.

FIG. 11. Calculated absorption spectra for ensembles of InAs quantum dots with mean diameters of (a) 23.9, (b) 30.3, (c) 36.6 and (d) 42.2Å. (a) shows ensemble spectra for size distributions with 0, 5 and 10% standard deviations. (b), (c) and (d) show only the spectra associated with a 5% size distribution. The labels (a)-(k) refer to the classification of the states in Table VI.

FIG. 12. Pseudopotential calculated (circles) positions of absorption peaks minus the band gap *vs* band gap for InAs quantum dot ensembles with mean diameters of 23.9, 30.3, 36.6 and 42.2Å and standard deviations of 5%. The pseudopotential results are connected using the analysis from section III C. The labels (a)-(k) refer to the classification of the states in Table VI. Experimental results from Ref. [11] are represented by the black lines.

Fig. 1

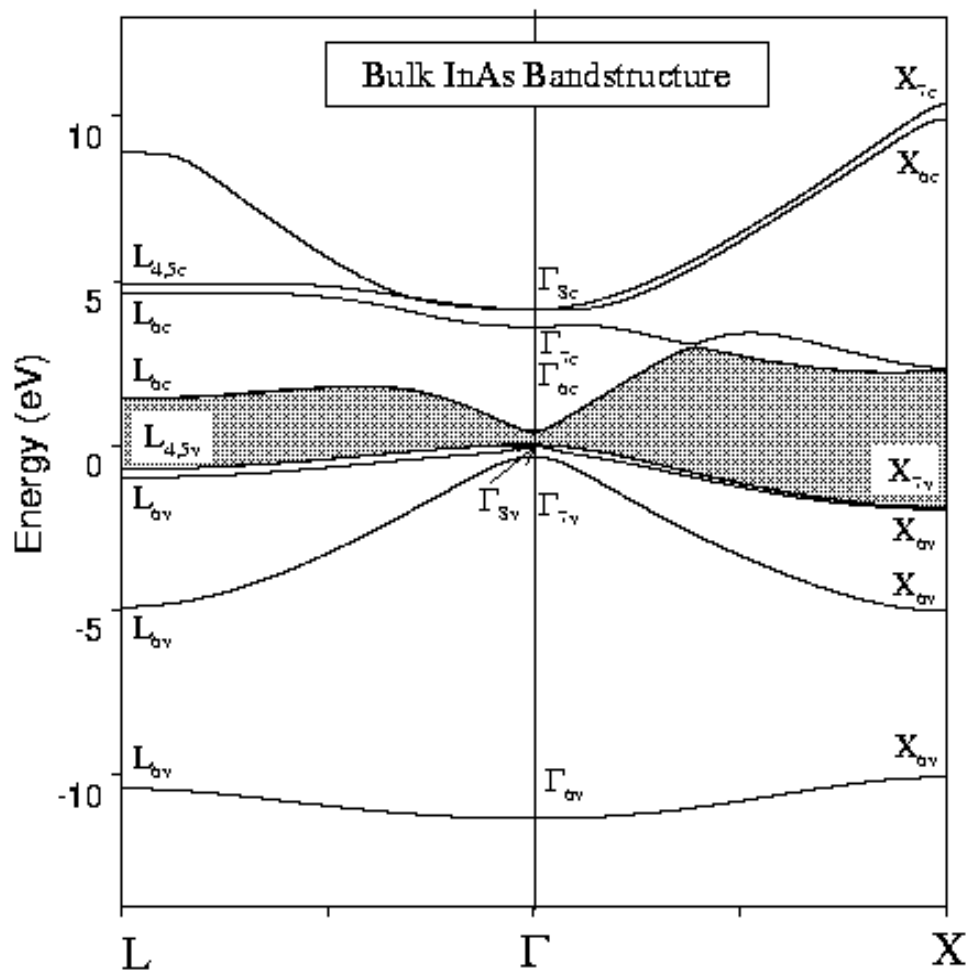


Fig. 2

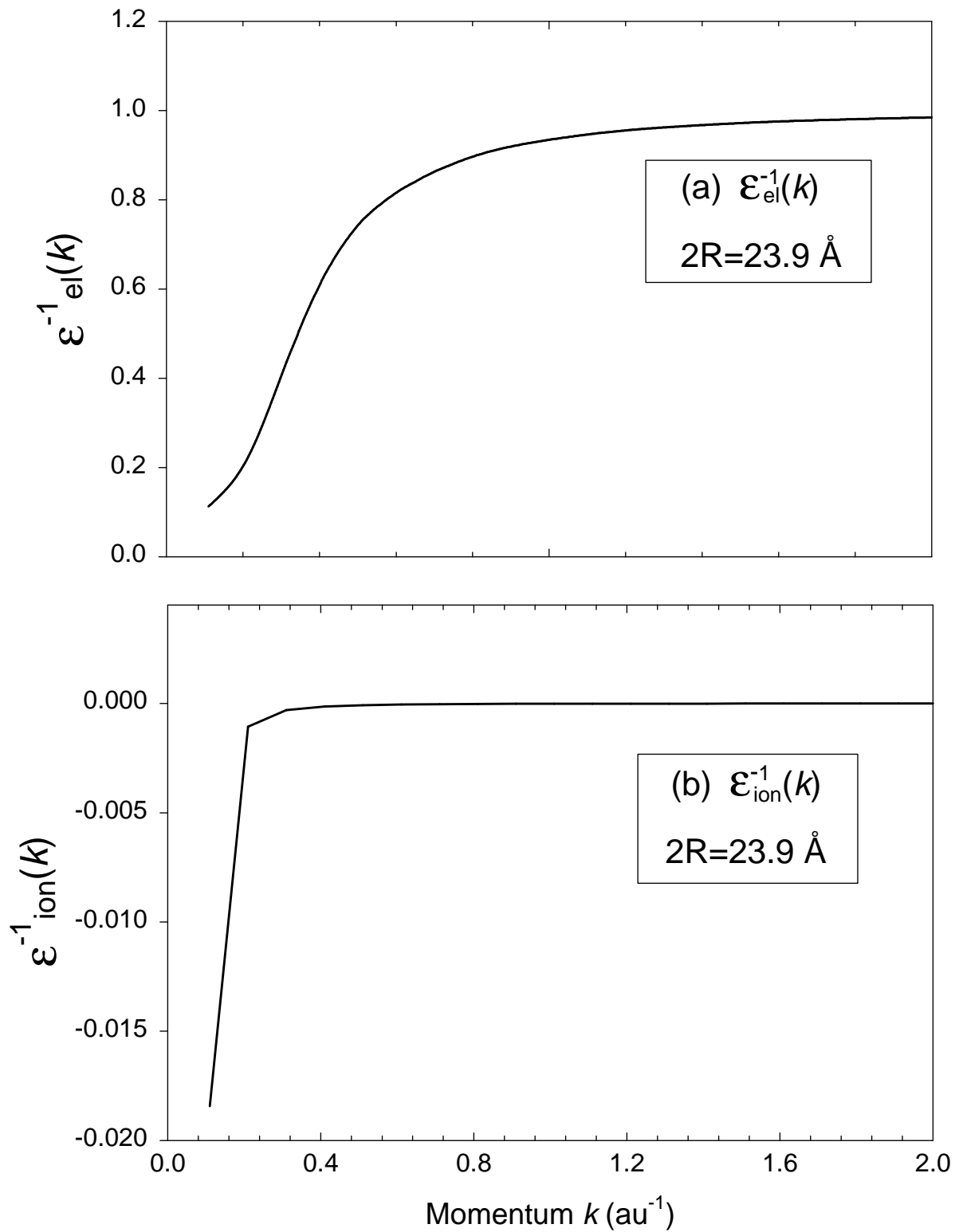


Fig. 3

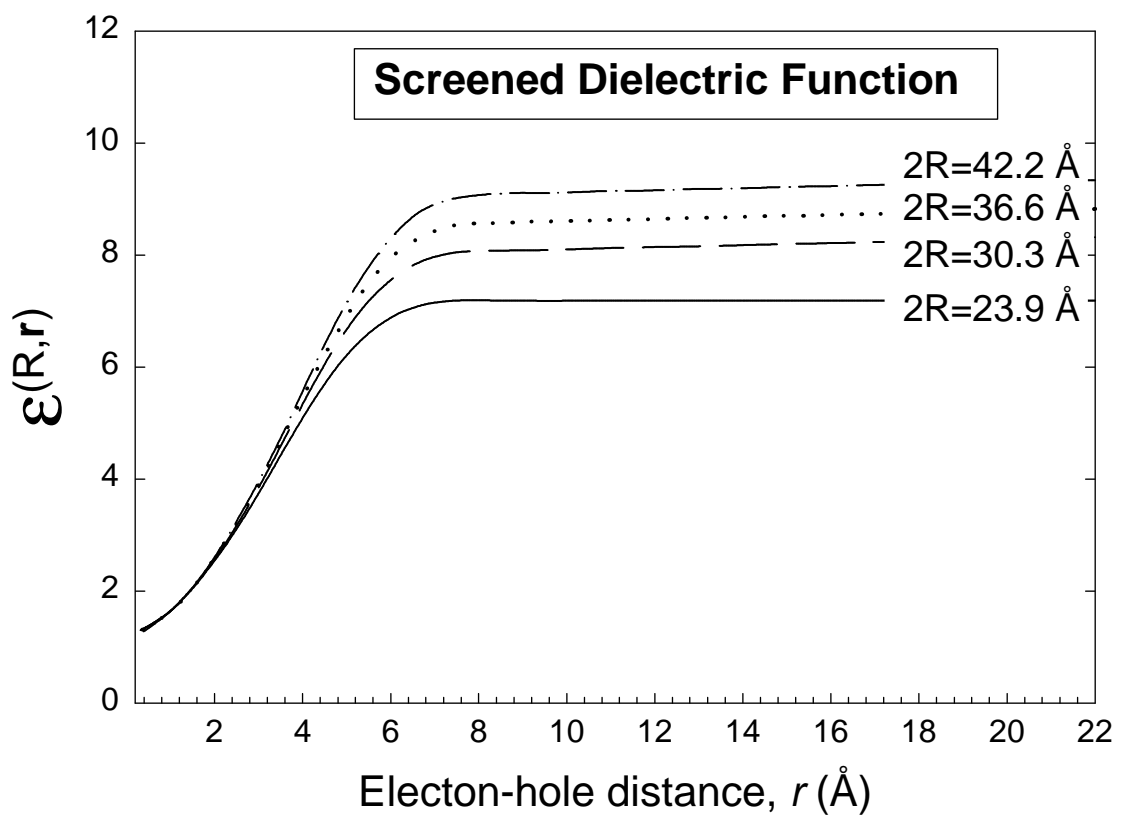


Fig. 4

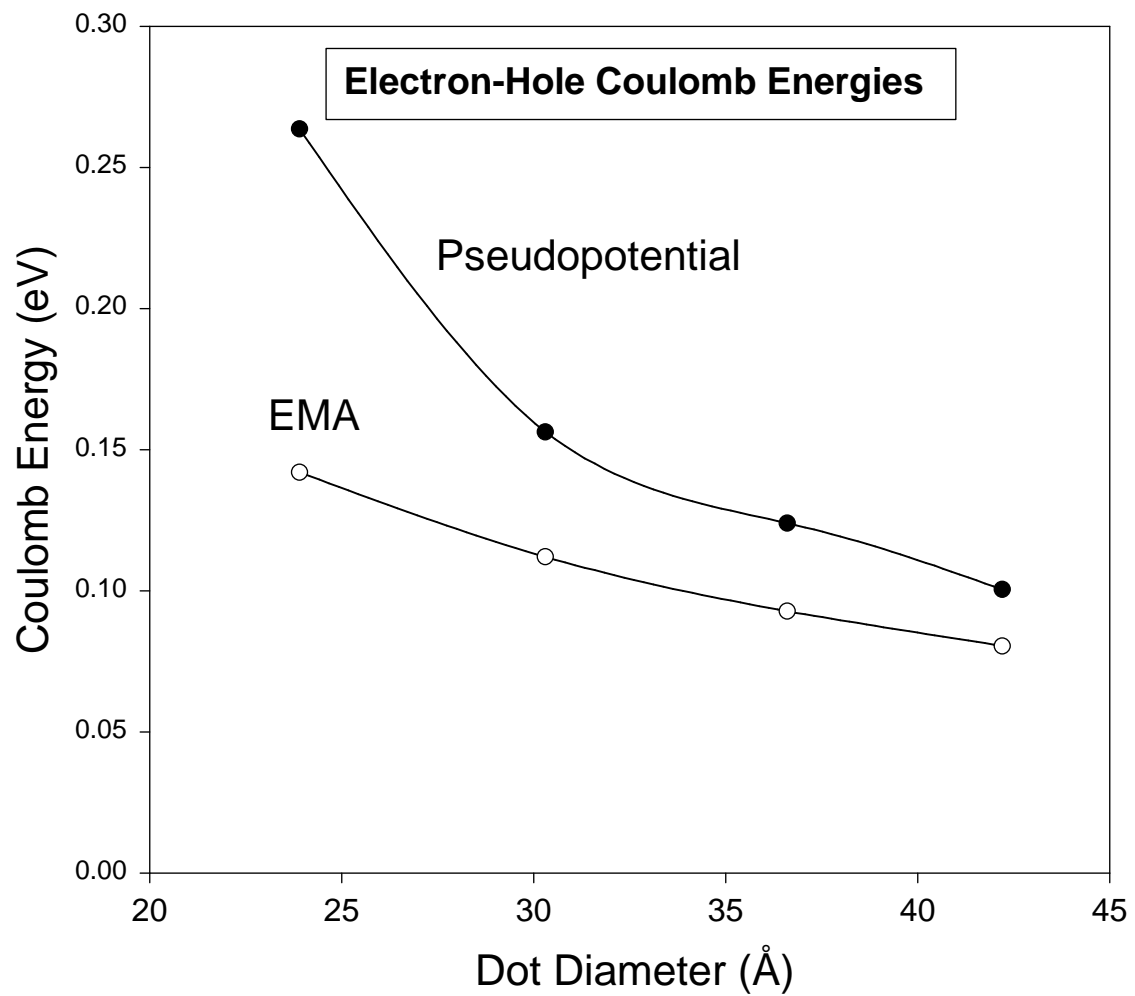


Fig. 5

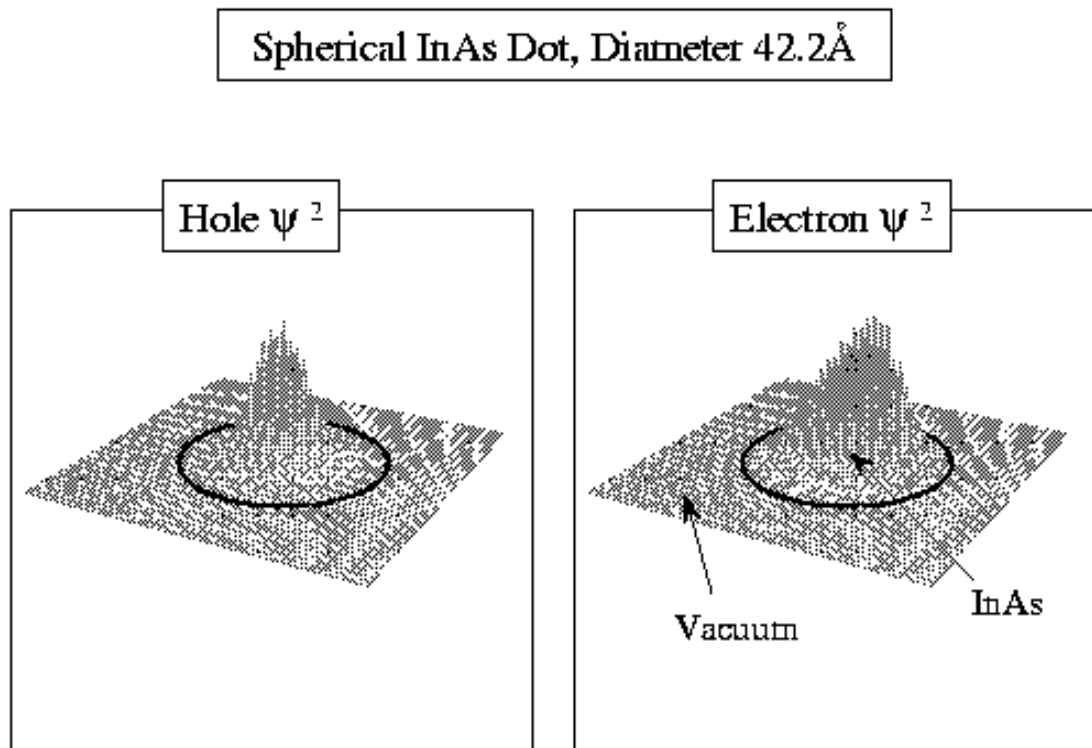


Fig. 6

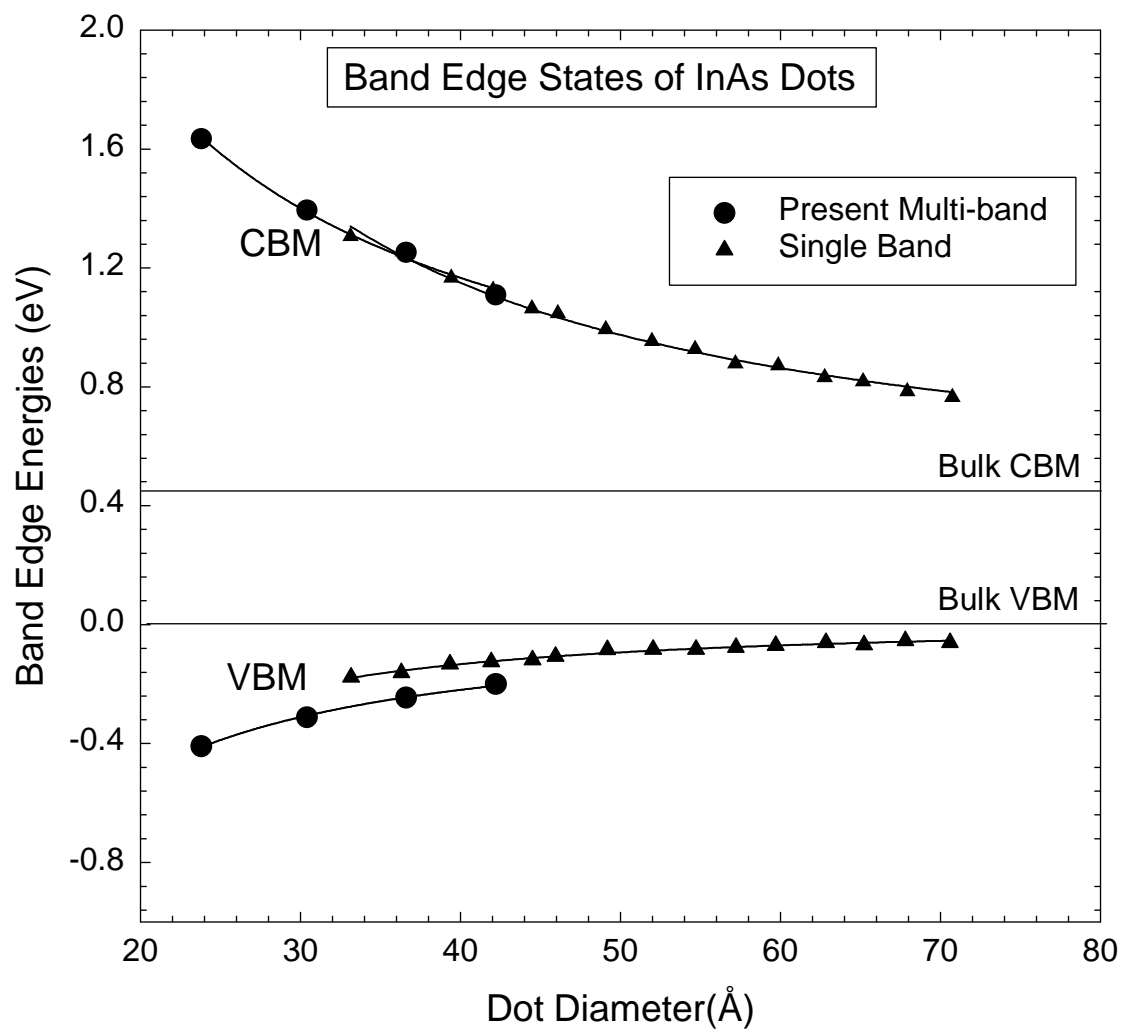


Fig. 7

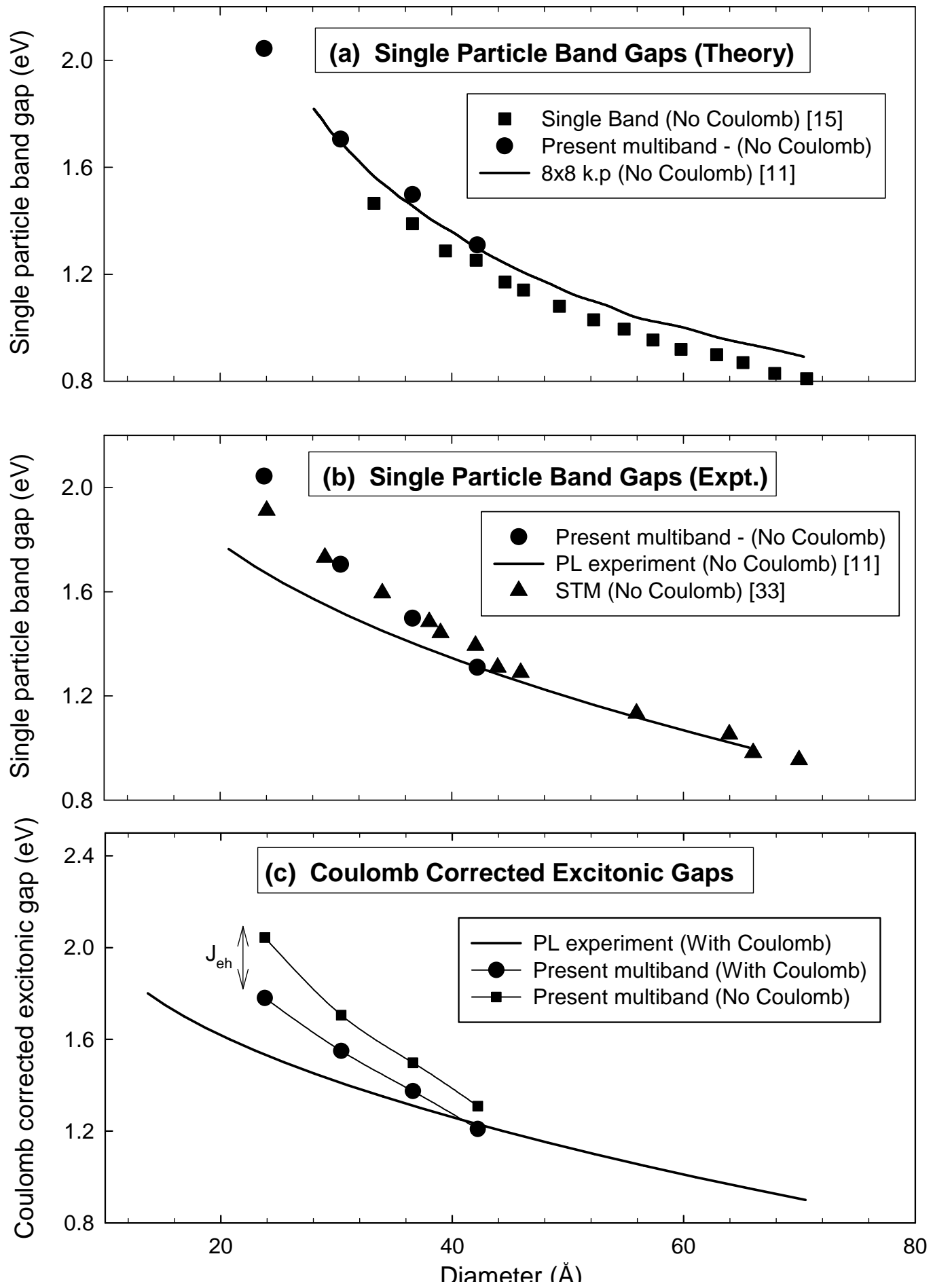


Fig. 8

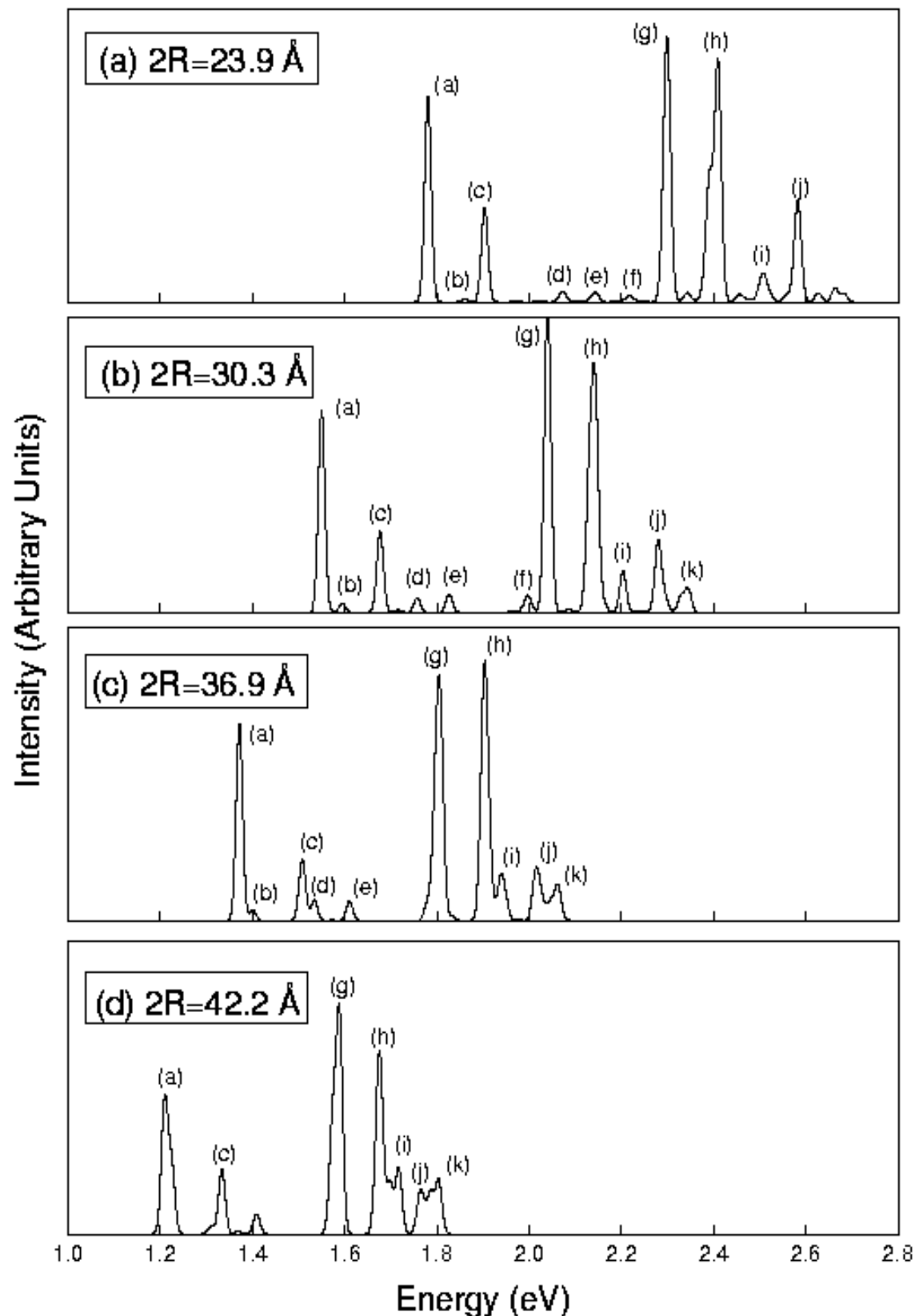


Fig. 9

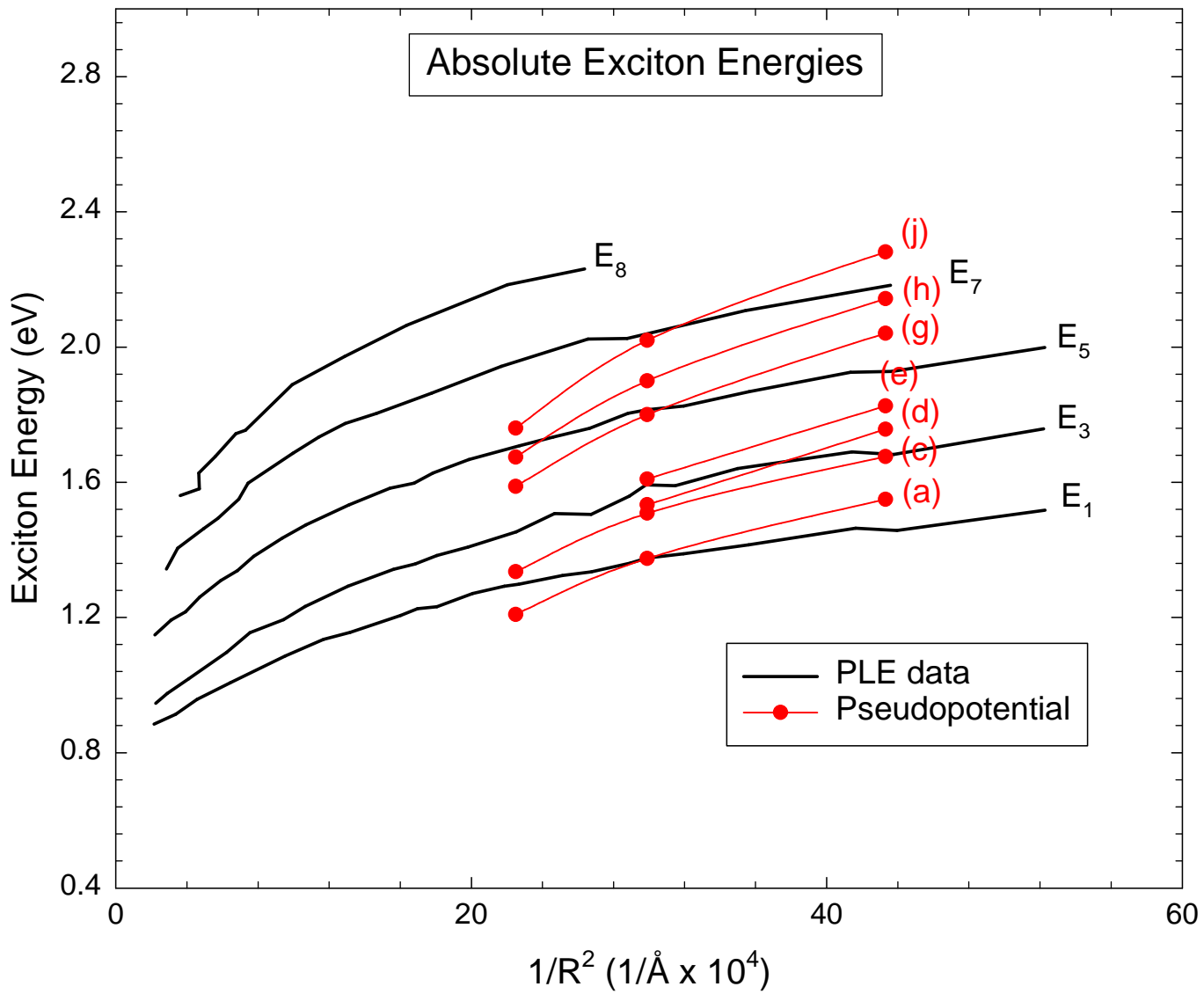


Fig. 10

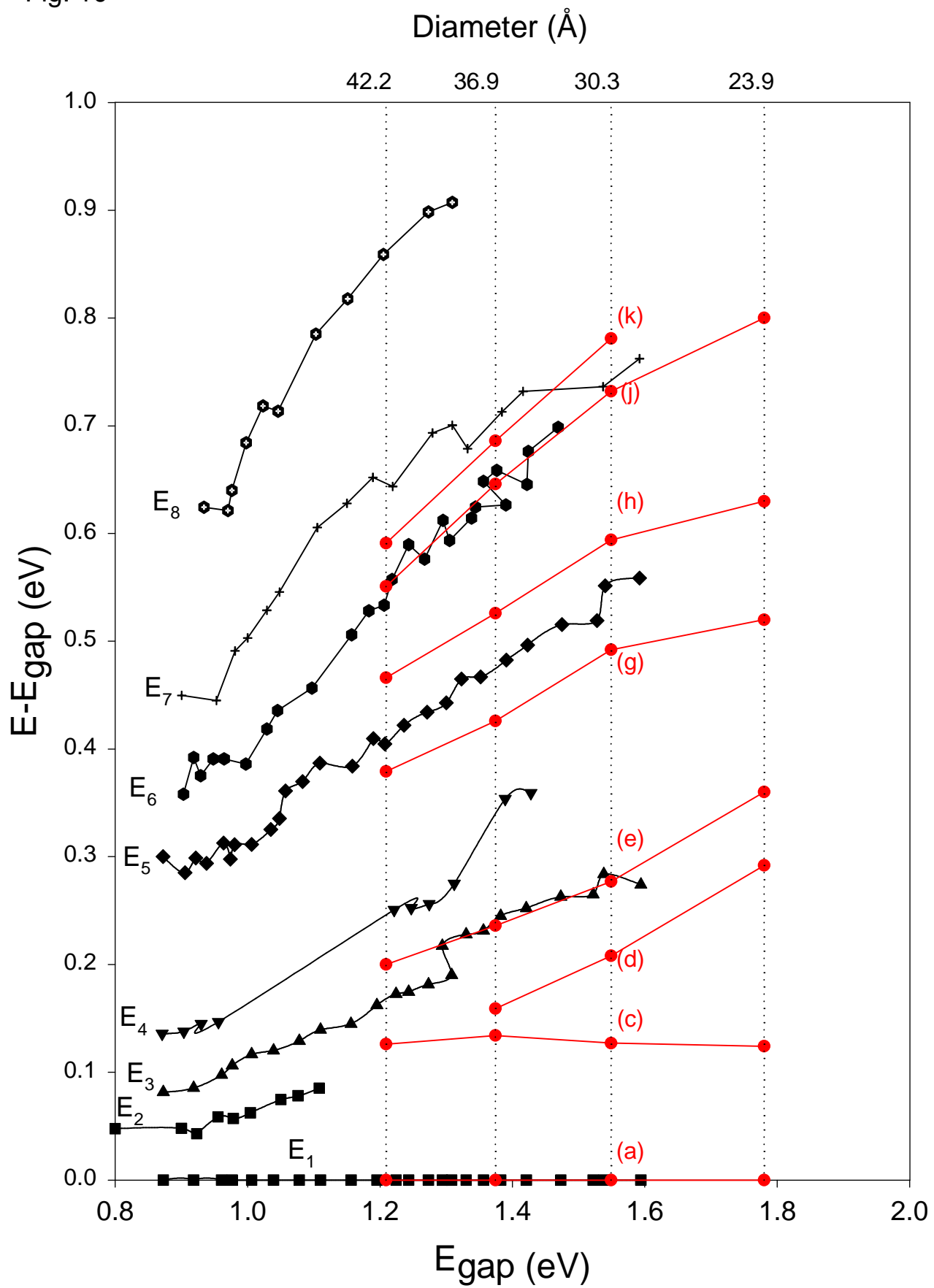


Fig. 11

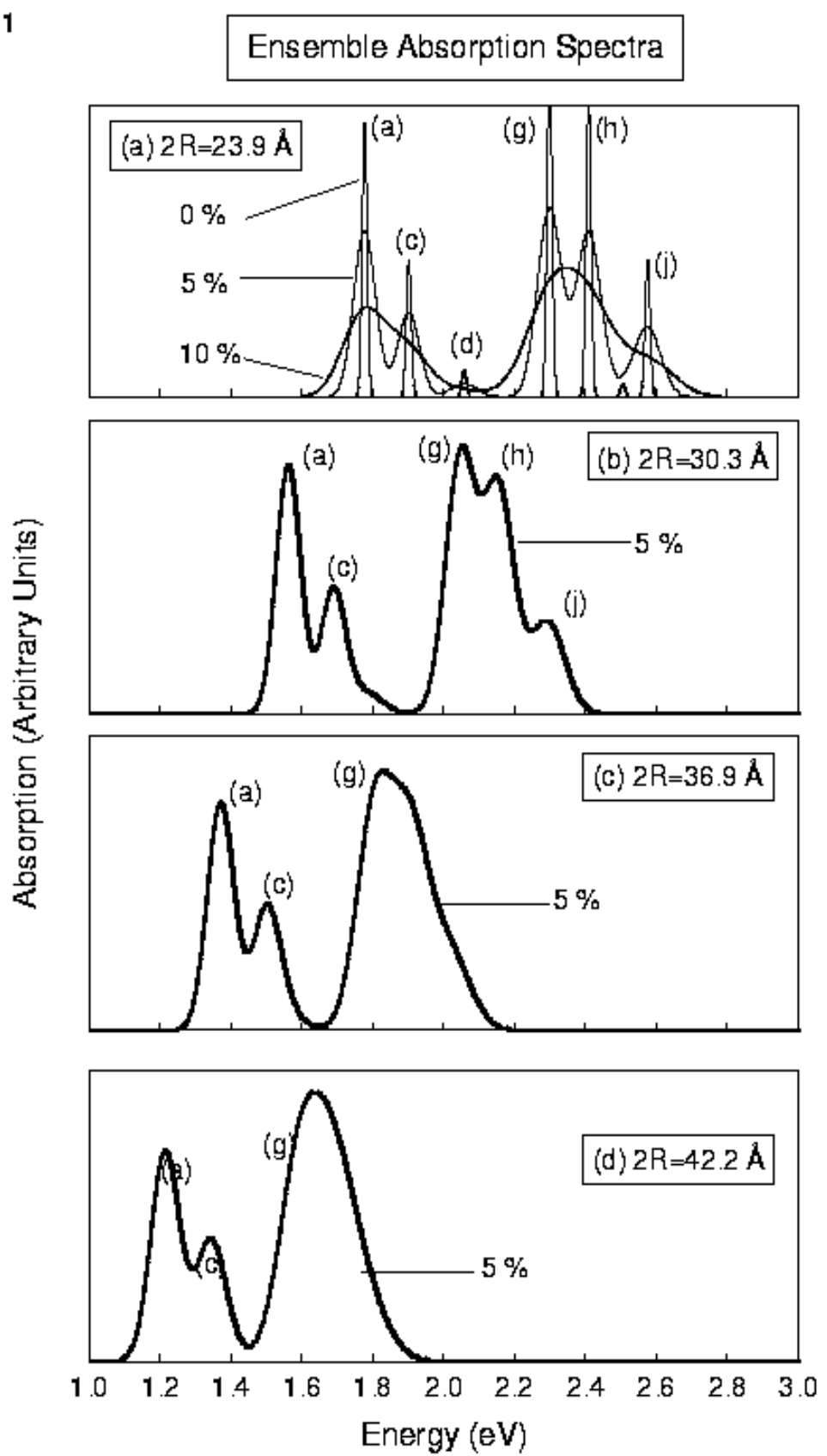


Fig. 12

